JGR Solid Earth

RESEARCH ARTICLE
10.1029/2024JB029975

Key Points:
- We can use average values of velocity and particle volume fraction (or of mixture density and mass flux) to compute vertical profiles
- We use vertical profiles to compute fluxes, calculate correction coefficients, and transition from 2D to 2.5D models for better accuracy
- We compute dynamic pressure profiles and their maximum values, showing underestimation with constant profiles used in hazard assessment

Correspondence to:
M. de' Michieli Vitturi and B. Keim,
mattia.demichielivitturi@ingv.it;
bykeim@buffalo.edu

Citation:
Keim, B., & de' Michieli Vitturi, M. (2025). Beyond the average: Computation of vertical profiles in dilute pyroclastic density currents and their use in shallow-water models. *Journal of Geophysical Research: Solid Earth*, *130*, e2024JB029975. https://doi.org/10.1029/2024JB029975

Received 24 JUL 2024
Accepted 7 DEC 2024

Author Contributions:
Conceptualization: B. Keim, M. de' Michieli Vitturi
Methodology: B. Keim, M. de' Michieli Vitturi
Software: B. Keim, M. de' Michieli Vitturi
Supervision: M. de' Michieli Vitturi
Validation: B. Keim, M. de' Michieli Vitturi
Writing – original draft: B. Keim, M. de' Michieli Vitturi

Beyond the Average: Computation of Vertical Profiles in Dilute Pyroclastic Density Currents and Their Use in Shallow-Water Models

B. Keim[1] **and M. de' Michieli Vitturi**[2]

[1]Department of Geology, University at Buffalo, Buffalo, NY, USA, [2]Istituto Nazionale di Geofisica e Vulcanologia, Sezione di Pisa, Pisa, Italy

Abstract Pyroclastic density currents (PDCs) present significant hazards due to their high temperatures and dynamic pressures. Accurate estimation of dynamic pressure, vital for assessing potential damage, requires knowledge of the vertical variations of velocity and particle concentration within the PDC, particularly in the first few meters of the flow above the ground. Existing approaches to dynamic pressure calculations used in hazard assessment are often based on average values for velocity and particle volume fraction. These average values may misrepresent the flow dynamics, especially near the base of the flow where the gradients of flow variables are larger. Here, we present a new, physically based approach that allows for the calculation of the vertical profiles of velocity and concentration from a combination of depth-averaged values for these properties and non-dimensional flow parameters. Finally, we demonstrate the use of these profiles within an existing shallow-water model and show its potential applications toward probabilistic hazard assessment.

Plain Language Summary Pyroclastic density currents pose a significant threat due to their high dynamic pressure—the forceful impact they exert. Assessing this pressure requires an understanding of the vertical variations in both velocity and particle volume fraction within the current, particularly in the lower regions of the flow where the dynamic pressure is at its maximum. However, current hazard assessment methods often rely on averaged values for these parameters, which can misrepresent flow dynamics, especially close to the ground. To address this limitation, we present novel, physically based profiles that enable more accurate calculations of the vertical variations of velocity and concentration. Our approach uses the average values and non-dimensional flow parameters to calculate these profiles. We then apply these new profiles to an existing model and show its potential application for hazard assessment.

1. Introduction

Pyroclastic density currents (PDCs) are among the most hazardous volcanic phenomena, posing significant risk to communities residing near volcanic edifices. These flows, comprised of hot pyroclastic material, gases, and lithic clasts, exhibit rapid propagation and can generate large dynamic pressures and maintain elevated temperatures at large distances from their source (Dufek et al., 2015; Jones et al., 2023; Pensa et al., 2023; Sigurdsson et al., 2015). Originating from diverse volcanic processes such as Plinian and sub-Plinian column collapses, lava dome failures, hydrothermal explosions, and lateral blast eruptions, PDCs demonstrate varied behaviors governed by particle volume fraction. Dense, particle-rich (with >10% particle volume fraction) flows, for example, the 1902 eruption of Mount Pelee, or the 1991 eruption of Mount Unzen, Japan, propagate in a manner similar to debris flows. In contrast, dilute pyroclastic surges (with typically <1% particle volume fraction) such as the eruptions of Mount Ontake, Japan (2014), Chichon, Mexico (1982), Vesuvius, Italy (August 25th, 79 CE) and Taal, Philippines (2020), exhibit density stratification with a more concentrated basal flow underlying a suspended fine ash unit, which represents 90%–95% of the total particles in the current (Dellino et al., 2019; Doronzo et al., 2022; Lagmay et al., 2021; Neri et al., 2022; Valentine, 1998). These dilute flows can also form as overlying currents from their dense counterparts and result in strong density stratification (e.g., Lube et al., 2020). Pyroclastic surges, which are responsible for the majority of volcanic fatalities, are highly mobile and are capable of overcoming topographic barriers (Dellino, Dioguardi, Isaia, et al., 2021; Lube et al., 2015; Pensa et al., 2023; Swanson et al., 2015), with particle-particle interactions and turbulent dynamics playing key roles in their transport and deposition (e.g., Roche, 2012).

Table 1
Dynamic Pressure Effects on Structures, Adapted From Dellino, Dioguardi, Rinaldi, et al. (2021)

Dynamic pressure effects	
$P_{dyn} (kPa)$	Effect on structures
<1	No damage expected
$1 \leq 5$	Openings may break
≥5	Walls begin to break

The effect of a pyroclastic surge on infrastructure is a function of both the flow temperature and dynamic pressure (Dellino, Dioguardi, Isaia, et al., 2021; Pensa et al., 2023). The dynamic pressure, which is the pressure acting on buildings or people, is calculated as

$$P_{dyn} = \frac{1}{2}\rho_{mix}U^2, \tag{1}$$

with mixture density ρ_{mix} and current velocity U. Dynamic pressures higher than 5 kPa can produce significant damage, while pressures under 1 kPa have minimal to no consequence on buildings and infrastructure (Dellino, Dioguardi, Isaia, et al., 2021) (Table 1). Particle volume fraction within the flow is a critical parameter since it is the largest influence on the mixture density, and thus the dynamic pressure.

In addition to high dynamic pressures, PDCs in the proximal areas of a volcano can have a high concentration of hot pyroclastic material that contributes to a high flow temperature. This combination of high dynamic pressures and temperatures can burn buildings, break windows or entryways, and knock over walls. The specific combination of temperature and dynamic pressure is a key parameter in estimating the survivability of these flows (Dellino, Dioguardi, Isaia, et al., 2021). Because of these hazards and their impact on human survivability estimations, particularly related to the dynamic pressure of the flow, it is therefore critical to accurately estimate the particle volume fraction and velocity in the region within a few meters from the ground, since the dynamic pressure P_{dyn} has a maximum in this region (Dellino, Dioguardi, Isaia, et al., 2021). The variables that define the dynamic pressure are not constant with flow height, and thus the values obtained by using depth-averaged values of the velocity and the density (e.g., those produced by shallow-water models) can over/underestimate it. Therefore, it is important to have a physical basis for the velocity and concentration profiles, rather than using an average value for the purposes of hazard assessment.

The flow velocity is highly non-linear from the base to the top of the flow (Jones et al., 2023). General trends for velocity and concentration within dilute flows can be seen in Figure 1, where the velocity increases from zero at the base of the flow (no-slip condition), and the concentration profile has a maximum at the lower flow boundary and decreases with height from the ground. These general trends are used in many dilute PDC models (e.g., Dioguardi & Dellino, 2014; Dioguardi & Mele, 2018; Valentine, 1987) due to their relative ease of use in modeling exercises. Previous work related to velocity profiles in PDCs (e.g., Dellino, Dioguardi, Isaia, et al., 2021; Dioguardi & Dellino, 2014; Dioguardi & Mele, 2018; Valentine, 1987) has assumed a velocity profile based on the law of the wall. This law, originally developed by Von Kármán (1931), gives a good approximation of the entire velocity profile for natural flows, under the assumption of high Reynolds numbers, and predicts a velocity that increases logarithmically with distance from the lower flow boundary. In recent works (e.g., Dioguardi & Dellino, 2014; Dioguardi & Mele, 2018), the velocity profile is defined as

$$u(z) = u_*\frac{1}{\kappa}\ln\frac{z}{k_s} + 8.5 \tag{2}$$

with $u(z)$ as the time-averaged velocity, which is a function of height z above the ground, u_* is the flow shear velocity, κ is the Von Kármán constant (taken as $\kappa = 0.4$), k_s is the height of roughness elements along the basal boundary, and the additive constant 8.5 derives from experimental fitting. The vertical profile of concentration for each class of particles in these works is based on the Rouse number P_n (Rouse, 1937), defined as $P_n = \frac{w}{\kappa u_*}$, with particle settling velocity w. The Rouse number represents the ratio of particle settling velocity to the shear velocity of the flow. The vertical concentration is typically defined (e.g., Valentine, 1987) as

$$C(z) = C_0\left(\frac{z_0}{H - z_0}\cdot\frac{H - z}{z}\right)^{P_n}. \tag{3}$$

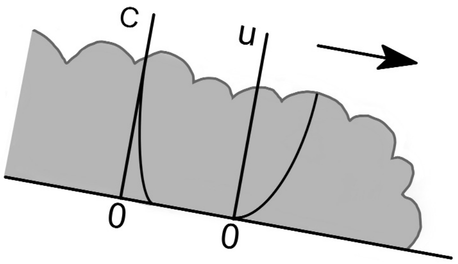

Figure 1. Illustrated cross section of a dilute flow with qualitative profiles for particle volume fraction C and velocity u. Adapted from Fagents et al. (2013).

This profile, known as the Rouse profile, assumes that there is a known concentration C_0 at a given flow reference height z_0, and a total flow height H. Quantitatively, the velocity profile begins at zero at the height of roughness elements k_s in the flow and increases toward the top of the flow. The concentration profile has a maximum at the base of the flow and decreases upward. Different profiles have been suggested for both the velocity and concentration, such as those in Cerminara et al. (2021), which are derived from large-scale experiments (e.g., E. C. Breard & Lube, 2017; Brosch & Lube, 2020; Esposti Ongaro et al., 2020). Their velocity profile is given as a power-Gaussian function combining a power-law profile in the inner layer with a Gaussian profile in the outer layer, ensuring a smooth and differentiable transition between the two regions. The concentration profile assumes that the solid mass fraction decreases exponentially with height, starting from a maximum value at the bottom surface. While these profiles are robust and fit experimental data well, here we present our methodology applied to the more "classical" profiles. The choice to use a "classical" vertical profile in this study is motivated by the need to relate the free parameters in the profile equations to depth-averaged flow variables. In the case of the "classical" profiles we adopted, we demonstrate how this relationship can be established, allowing the depth-averaged quantities to inform the profile parameters. For the profiles proposed by Cerminara et al. (2021), specifically the recommended velocity profile, it is straightforward to compute depth-averaged values from the vertical profile. However, establishing a reverse relationship, where depth-averaged flow variables determine the free parameters of the profile, is not readily apparent. This limitation informed our decision to proceed with the "classical" profiles.

In the next sections, we modify Equations 2 and 3 and present the derivation of the equations for the vertical profiles of velocity and concentration. We also introduce a Python tool that computes these profiles, as well as the total grain size distribution (TGSD). Then, we apply the computed vertical profiles to an existing shallow-water model, IMEX-SfloW2D (de' Michieli Vitturi et al., 2023). While we present this application as an example, this approach is not tied to a specific depth-averaged model, but could be used also with other codes. We modify the flux terms of the shallow-water equations to account for the assumed vertical profiles, and describe the steps involved in computing the flux modifying coefficients. We then compare, for both a 1D test case on a constant slope and a 2D test case on a real topography, the output of the original depth-averaged model with that of the updated version that includes vertical profiles for velocity and particle volume fraction. For both the cases, the differences in the dynamic pressure values computed by the models are discussed.

2. Methods

In this section we describe the approach used to compute the velocity and concentration profiles, where concentration refers to the particle volume fraction. It is important to note that these profiles represent a significant simplification of the problem at hand. In reality, dynamic pressure energy is mostly transported by large-scale turbulent structures and gravity waves (Brosch et al., 2021), and in a turbulent flow, the vertical profiles change continuously with time, and what we present are approximations of the time-averaged profiles—where the temporal fluctuations associated with turbulence are neglected.

2.1. Velocity Profile Derivation

Following the approach of Valentine (1987) and Dellino, Dioguardi, Isaia, et al. (2021), we assume the velocity above the bed being defined by a logarithmic profile, based on the assumption of a turbulent flow. The velocity profile in the turbulent boundary layer is primarily based on the law of the wall, which has been verified experimentally and is commonly applied to dilute PDC modeling (e.g., Valentine, 1987). With respect to previous work, where a singularity is present at the base of the profile in the turbulent boundary-layer region, here we adopt a formulation based on the Prandtl-Von Kármán universal velocity-distribution law (Dingman, 1984), which results in a no-slip condition ($u(0) = 0$) at the base of the flow:

$$u(z) = \frac{u_*}{\kappa}\ln\left(\frac{30z}{k_s} + 1\right). \tag{4}$$

The shear velocity u_* (for steady, uniform flow, of approximately constant depth) can be expressed as a function of basal shear stress τ_b and depth-averaged density $\overline{\rho}$ as

$$u_* = \sqrt{\frac{\tau_b}{\overline{\rho}}}. \tag{5}$$

From the shear stress form of the Darcy-Weisbach equation (Chaudhry, 2014), the bed shear stress τ_b can be expressed in terms of $\overline{\rho}$, the depth-averaged flow velocity $\overline{U}$, and a friction factor C_f as

$$\tau_b = C_f \cdot \overline{\rho} \cdot \overline{U}^2. \tag{6}$$

Then, combining Equations 5 and 6, the shear velocity can be written as:

$$u_* = \overline{U}\sqrt{C_f}. \tag{7}$$

and, substituting the expression of the shear velocity in Equation 4, the velocity profile in the turbulent boundary-layer region can be written as

$$u(z) = \overline{U}\,\frac{\sqrt{C_f}}{\kappa} \cdot \ln\left(\frac{30z}{k_s} + 1\right). \tag{8}$$

This velocity profile is similar to that in Dellino, Dioguardi, Isaia, et al. (2021) but here, as written above, the velocity tends to zero at the base of the flow, when $z \to 0$. For the velocity profile, we want the depth-averaged value to be equal to $\overline{U}$, that is,:

$$\int_0^H u(z)dz = \overline{U}, \tag{9}$$

where H is the flow thickness. In order to satisfy this condition, differing from previous work, here we also allow for the presence of a free-stream region, where velocity is assumed to be constant. The thickness of the turbulent boundary layer and the presence (or absence) of a free-stream region depends on several factors. It can be shown that there exists a critical flow thickness H_{crit}, above which a free-stream region is required to have the depth-averaged velocity profile equal to $\overline{U}$, while below the critical thickness the velocity has a logarithmic profile for the entire flow thickness. This critical thickness is given by

$$H_{crit} = \frac{k_s}{30}\left(\frac{a}{\mathcal{W}(-ae^{-a})} - 1\right), \tag{10}$$

where $a = \frac{\kappa}{\sqrt{C_f}}$ and $\mathcal{W}$ is the Lambert function, which is more thoroughly described in Appendix A. These two cases for the velocity profile are presented here, with details of the derivation of the boundary layer height d_{bl} presented in Appendix A.

Case 1. For a flow with thickness H smaller than the critical thickness H_{crit} (Figure 2, left), velocity is computed as

$$u(z) = u_{coeff} \cdot \overline{U} \cdot \frac{\sqrt{C_f}}{\kappa} \cdot \ln\left(\frac{30z}{k_s} + 1\right) \qquad \text{if} \qquad H \le H_{crit}, \tag{11}$$

where

$$u_{coeff} = \frac{\kappa}{\sqrt{C_f}}\left[\left(1 + \frac{k_s}{30 \cdot d_{bl}}\right) \cdot \ln\left(\frac{30 \cdot d_{bl}}{k_s} + 1\right) - 1.0\right]^{-1}. \tag{12}$$

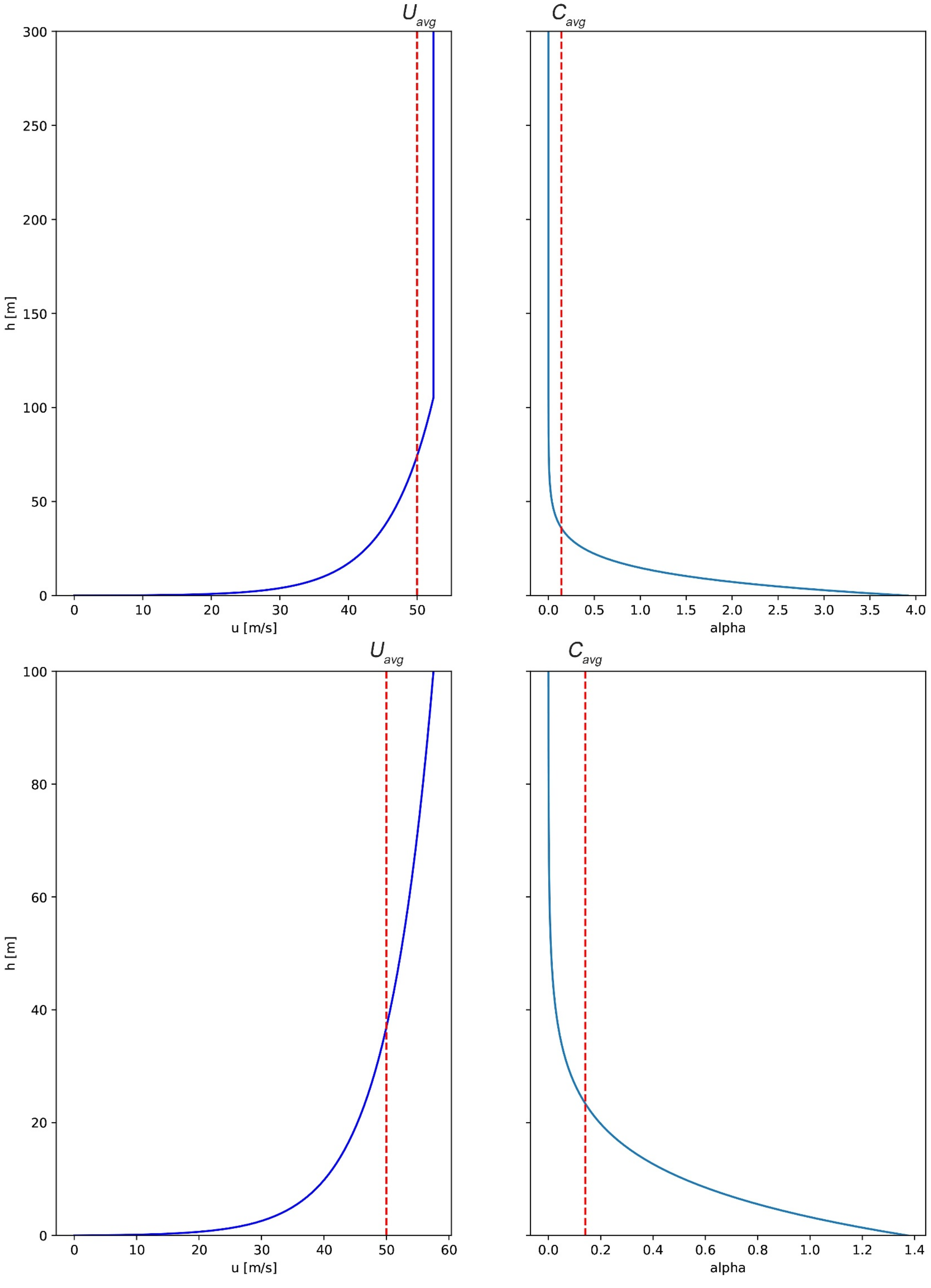

Figure 2. Plot of assumed vertical velocity and concentration profiles when $H \leq H_{crit}$ (left) and when $H \geq H_{crit}$ (right), calculated with a flow velocity of 50 m/s and particle volume fraction $\alpha = 1.41 \times 10^{-1}$.

With respect to Equation 8, here the profile is scaled by a factor u_{coeff} to ensure that the integral of the profile matches the depth-averaged velocity value. The log-profile region of the flow velocity for this case is shown in the left panel of Figure 2.

Case 2. For a flow with thickness H larger than the critical thickness H_{crit} (Figure 2, right), the velocity profile $u(z)$ is given by

$$u(z) = \begin{cases} \overline{U} \cdot \dfrac{\sqrt{C_f}}{\kappa} \cdot \ln\left(\dfrac{30z}{k_s} + 1\right) & \text{if } z \leq d_{bl}, \\ \overline{U} \cdot \dfrac{\sqrt{C_f}}{\kappa} \cdot \ln\left(\dfrac{30d_{bl}}{k_s} + 1\right) & \text{if } z > d_{bl}, \end{cases} \tag{13}$$

where d_{bl} represents the thickness of the turbulent boundary layer (Valentine, 1987). The boundary layer height d_{bl} is calculated as:

$$d_{bl} = -bk_s \cdot \mathcal{W}\left(-\frac{e^{\frac{a}{b}-\frac{1}{bc}}}{bc}\right) - \frac{1}{c}, \tag{14}$$

where $\mathcal{W}$ is the Lambert-W function and where $a = \frac{\frac{H}{k_s}\sqrt{C_f}}{\kappa}$, $b = \frac{1}{30} + \frac{H}{k_s}$, and $c = 30$ are non-dimensional parameters. The thickness of the turbulent boundary layer given by Equation 14 guarantees that the integral of the profile matches the depth-averaged velocity value. In this case, the velocity profile is composed of two regions: the log-based, turbulent boundary layer, which transitions to the free-stream velocity region at and above the boundary layer height d_{bl}. Note that d_{bl} is distinct from H_{crit}.

2.2. Concentration Profile Derivation

Several works have used a profile derived from the Rouse number P_n to describe particle volume fraction within a turbulent flow (e.g., Dellino, Dioguardi, Isaia, et al., 2021; Middleton & Southard, 1977; Valentine, 1987). The Rouse profile, as defined by Equation 3, relates the concentration of particles within the flow with the ratio of settling velocity to shear stress, and assumes that there is a known concentration C_0 at a given flow reference height z_0. However, the profile is not a function of the depth-averaged concentration $\overline{C}$ and, setting the depth-averaged value of $C(z)$ equal to $\overline{C}$, we obtain an equation relating C_0 and z_0. By fixing a value for C_0, it is possible that for small values of $\overline{C}$ there are no values of z_0 between 0 and H satisfying this equation. Similarly, by fixing the reference relative height z_0, it is possible that the concentration value C_0 is no longer bounded between 0 and 1. For this reason, we propose a modified concentration profile which is based on the Rouse number and a relationship between mass and momentum diffusivity, that can be written in terms of depth-averaged flow variables. Similarly to the velocity profile, the concentration profile contains a gradient close to the base of the flow with an overlying free stream region, where particle volume fraction is assumed to be constant due to particle settling counteracted by sediment transport via turbulent fluctuations.

The concentration profile is controlled by the sediment mass diffusivity ϵ_s, which is assumed here to satisfy a linear relationship with momentum diffusivity ϵ_m. As a consequence, the concentration boundary layer, defined as the region of the flow in which a particle volume fraction gradient exists, corresponds to the turbulent boundary layer. In this layer, in equilibrium conditions (e.g., over very short timescales), the downward flux of solid particles due to gravitational settling q_{down} is balanced by the upward flux q_{up} of particles from turbulence, resulting in

$$q_{down} = q_{up}. \tag{15}$$

The downward flux of solids $\left(q_{down}\right)$, per unit area of a plane parallel to the bed, is given by:

$$q_{down}(z) = C(z) \cdot w \cdot (1 - C(z))^{1.5}, \tag{16}$$

where the last term accounts for hindered settling (as the concentration increases, this reduces the downward flux). The upward flux $\left(q_{up}\right)$ of solids due to turbulent diffusion is proportional to the concentration gradient through the sediment mass diffusivity ϵ_s, given by:

$$q_{up}(z) = -\epsilon_s \cdot \frac{dC(z)}{dz}. \tag{17}$$

The choice of ϵ_s significantly influences the concentration profile within the flow. Specifically, when ϵ_s varies linearly within the boundary layer, ranging from a maximum value at the bottom to zero at the top, the resulting concentration profile follows the Rouse profile. However, when a constant value is employed for ϵ_s, an exponential concentration profile is generated instead. In this study, the aim is to obtain a concentration distribution that diminishes exponentially with height, as indicated by findings from large-scale experiments reported by Cerminara et al. (2021). Hence, we adopt a constant value for ϵ_s to achieve this desired concentration profile:

$$\epsilon_s = \beta_{sm}\kappa u_* \left(\frac{d_{bl}}{6} + \frac{k_s}{60}\right), \tag{18}$$

where β_{sm} is the Schmidt number. Equation 18 is based on the assumption of a linear relationship between mass and momentum diffusivity and on the logarithmic velocity profile presented in the previous section. A detailed derivation is given in Appendix A.

Using the value of ϵ_s in Equation 17 makes the equation for the concentration profile given by Equation 15 a constant coefficients first order differential equation whose solution decreases exponentially with height:

$$C(z) = C_{coeff} \cdot e^{-\frac{\kappa u_* P_n}{\epsilon_s} \cdot z}, \tag{19}$$

in this equation C_{coeff} is an integration constant, whose value is determined to make the depth-averaged value of $C(z)$ equal to $\overline{C}$:

$$\overline{C} = \frac{1}{H}\int_0^H C(z)\,dz = C_{coeff}\frac{1}{H}\int_0^H e^{-\frac{\kappa u_* P_n}{\epsilon_s} \cdot z} dz. \tag{20}$$

Similar to the velocity profile, we now have two cases for the concentration profile.

Case 1: $H < H_{crit}$

For this case, the exponential concentration profile is defined for the whole flow thickness, and the free-stream region is absent. The concentration profile is then given as:

$$C(z) = \overline{C}C_{coeff} \cdot e^{-\frac{\kappa u_* P_n}{\epsilon_s} \cdot z} \qquad \text{for} \qquad 0 \le z \le H. \tag{21}$$

Please note that the integration constant has been rewritten as $\overline{C}C_{coeff}$, to make explicit the linear dependence of the concentration profile on the depth-averaged value. It is also worth to note that $C(0) = \overline{C}C_{coeff}$, and thus the coefficient C_{coeff} represents the ratio between the basal and depth-averaged concentrations.

Case 2: $H \ge H_{crit}$

For this case, we adopt a split profile with free-stream region, given by:

$$C(z) = \begin{cases} \overline{C}C_{coeff} \cdot e^{-\frac{\kappa u_* P_n}{\epsilon_s} \cdot z} & \text{for} \quad z < d_{bl}, \\ C(d_{bl}) & \text{for} \quad d_{bl} \le z \le H. \end{cases} \tag{22}$$

We thus assume a constant concentration in the free-stream region, with a concentration value equal to that at the top of the boundary layer. Equations 21 and 22 give the concentration at height z as a function of the depth-averaged concentration $\overline{C}$, the total flow thickness H, the boundary layer thickness d_{bl}, the particle Rouse number P_n, and the roughness height k_s. For both the cases, the calculation of the value of C_{coeff} as a function of the flow parameters is presented in Appendix A. It is important to observe that the equations can be used when classes of particles with different sizes (and thus different Rouse numbers) are considered. In this case, different profiles will be obtained for the different sizes, with different ratios between the depth-averaged concentrations and the basal concentrations.

3. Modeling Applications

3.1. Vertical Profiles Python Tool

The equations presented in the previous section (Equations 11–13, 21, and 22) provide the velocity and concentration profiles in terms of the depth-averaged values, non-dimensional numbers that can also be computed from the depth-averaged values, and additional constants specific to the flow and the topography. Therefore, it is useful to have a tool to compute the profiles once these parameters are given. A Python code for the computation of the vertical profiles is available on GitHub (https://github.com/BKeim-UB/SW_VERT_PROFILES). This tool computes the flow vertical profiles from the depth-averaged values, which can be the solid volume fraction $\overline{\alpha}_{s,tot}$ or the depth-averaged mixture density $\overline{\rho}$, and the mixture velocity $\overline{U}$ or the mixture momentum $\overline{\rho U}$. When the mixture momentum is given, due to the highly non-linear nature of the equations presented in the previous section, an iterative procedure is employed to compute $\overline{\rho}$, $\overline{U}$, and their vertical profiles. In this case, the Python tool initializes a guess for the depth-averaged velocity and starts an iteration loop. Within the loop, a function is called to compute the mixture density and the depth-averaged value of a flow property using the current guess of the depth-averaged velocity. The depth-averaged velocity is then updated using the computed values, and the process is repeated with the updated velocity to refine the estimate. An acceleration scheme is applied to improve the convergence of the iteration (Aitken, 1927). The loop continues until the convergence criteria are met or the maximum number of iterations is reached, at which point the final depth-averaged velocity is obtained. The capability to find the profiles when the depth-averaged mixture density and momentum are given is particularly relevant, because depth-averaged models solve for these variables, and thus the numerical implementation of the Python code can also be ported to these models.

The tool computes the concentration profiles not only for the solid phase as a whole, but also for the individual solid classes with different sizes and densities (and thus different settling velocities). Here, we assume the depth-averaged total grain size distribution (TGSD) being defined by a normal distribution in the Krumbein logarithmic phi scale, with mean μ and standard deviation σ, resulting in specific relative mass fractions on a binned phi scale. The tool then, from the computed concentration vertical profiles of the different classes, allows the user to compare the depth-averaged TGSD, the basal TGSD, and the bins relative mass fractions that are sedimented (lost) into the bedload region of the flow (from the settling velocities and bottom fractions of solid particles). It is important to note that the approach to compute the vertical profiles of the different classes works for any TGSD, and not only for a normal distribution, which has been chosen in the Python tool only to reduce the number of input parameters.

Figures 3 and 4 show the output of the tool for the following flow parameters: $h = 8$ m; $\overline{U} = 20$ m/s; $\overline{\rho}_m = 10$ kg/m^3; $\mu = 2$ and $\sigma = 1$ (the size distribution has been partitioned in 10 classes between -1 and 5).

The function computes the relative mass fractions of solid classes based on the parameters of a size distribution. Given a mean, standard deviation, and a list of bin edges, it uses a normal distribution function to compute the fraction of material in each class x_s as:

$$x_s = \Phi\big(0.5 \cdot (\phi_i + \phi_{i+1}), \mu, \sigma\big) \quad \text{for } i = 1, \ldots, (n_{bins} - 1). \tag{23}$$

The density of solid particles is assumed to change linearly in the phi scale between a minimum a maximum value (Bonadonna & Phillips, 2003):

$$\rho(\phi) = \begin{cases} \rho_1 & \text{if } \phi < \phi_1, \\ \rho_1 + \dfrac{\phi - \phi 1}{\phi_2 - \phi 1}\rho_2 & \text{if } \phi_1 \leq \phi \leq \phi_1, \\ \rho_2 & \text{if } \phi > \phi_2. \end{cases} \tag{24}$$

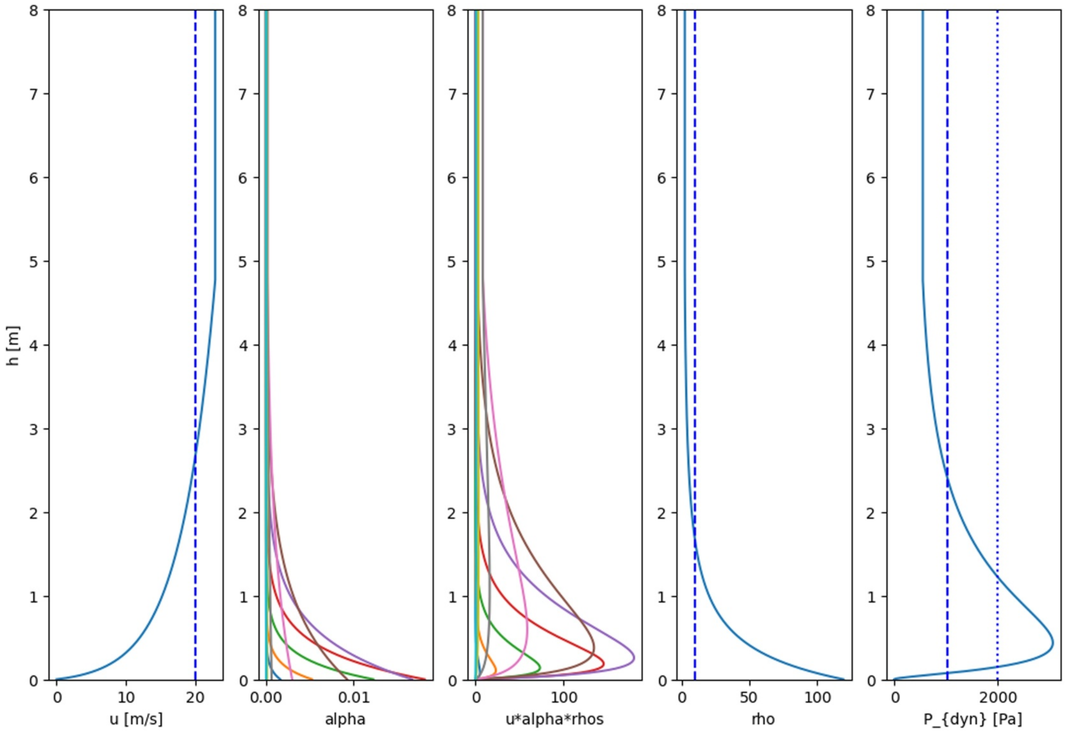

Figure 3. Vertical profiles for flow properties computed using supplemental Python tool. From left to right: velocity; particle volume fraction; the product of velocity, volume fraction, and density; density $\left(kg/m^3\right)$ and dynamic pressure. The solid lines and the dashed lines represent the vertical profiles and their averages, respectively. The dotted line for the dynamic pressure (last panel) is the value computed from the depth-averaged values of density and velocity. The different colors in the second and third panels are for the different classes of particle sizes.

For the test presented in Figures 3 and 4, $\phi_1 = -2$, $\rho_1 = 1000$ kg/m^3, while $\phi_2 = 3$ and $\rho_2 = 2200$ kg/m^3. Finally, the following values have been used for the other parameters needed to define the profiles: the friction factor is $C_f = 0.01$ and the substrate roughness is $k_s = 1.5$ m, chosen to represent the influence of vegetation or hummocky topography on the flow. The vertical profiles are presented in Figure 3. The first panel presents the vertical velocity profile (solid line) and depth-averaged value (dashed line), and it shows that for this case the profile consists of both a log-region (up to approximately 5 m) and a free-stream constant region. The second panel presents the concentration profiles for the different solid classes, with the finer particles having a smaller ratio between the bottom and the top values due to the lower settling velocity. The middle panel shows the mass fluxes of the different solid classes, which contribute to the horizontal mixture momentum. These profiles clearly show that the combination of the velocity and concentration profiles produces peaks above the ground, at different heights for the different solid classes. The vertical concentration profiles also result in the total mixture density profile (solid line) shown in the fourth panel, where the depth-averaged value is also shown (dashed line). In this case the density at the bottom is one order of magnitude larger than that at the top of the flow. Finally, the last panel shows the profile of the dynamic pressure (solid line), its depth-averaged value (dashed line) and the dynamic pressure value computed from the depth-averaged values of velocity and density, respectively (dotted line). This plot clearly highlights that the peak value of dynamic pressure can greatly exceed its depth-averaged value, and thus this latter value (as the values produced by depth-averaged codes) represents an underestimation of the maximum dynamic pressure. These results show a similar effect to recent experimental work by Brosch et al. (2021), where turbulent fluctuations deviating from mean values clearly show maxima in pressure two to three times greater than currently assumed mean values, although the source of the deviation from the mean values is different. Figure 4 shows the grain size distributions for the average deposit, the bottom layer, and the "lost" fraction that is sedimented into the deposit. The mean (μ) sizes (ϕ) are 2.00 for the average, 1.31 for the bottom, and 0.78 for the lost portion. These differences in mean size have important implications for understanding the relationship between the deposited sediment and the original sediment transported by the flow. The ratios between these mean sizes could be used to infer correction factors—by determining the mean grain size of a

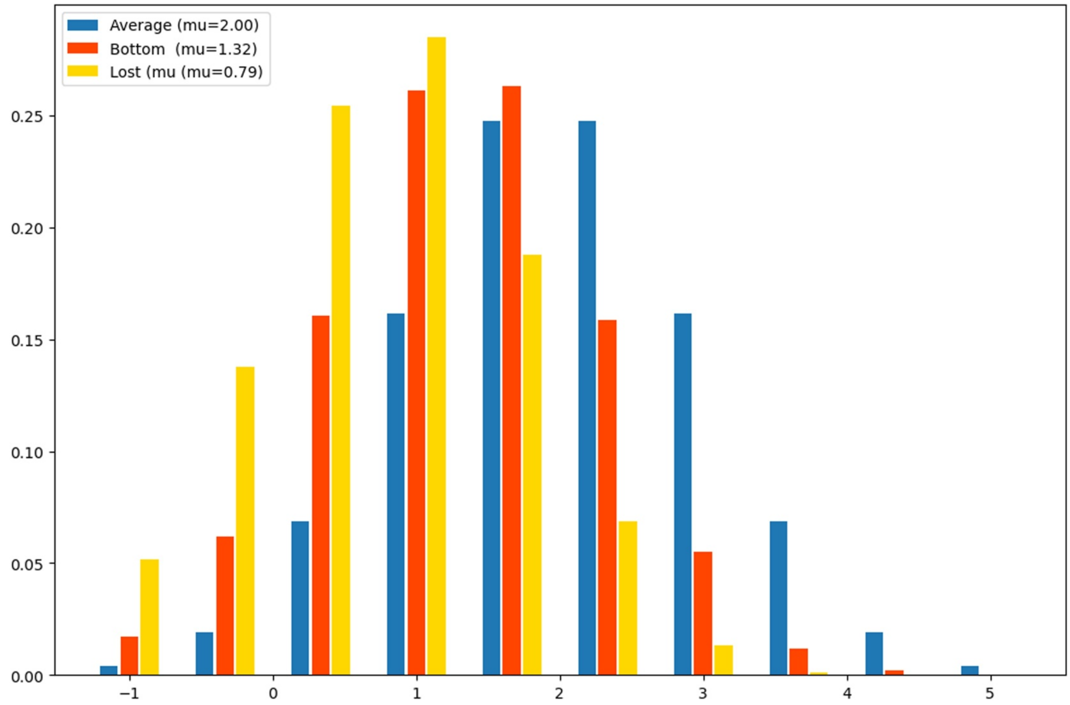

Figure 4. Average grain size distributions computed using supplemental Python tool, with the prescribed depth-averaged TGSD (blue), the TGSD at the bottom of the flow associate with the vertical profiles (red) and the TGSD of particles settling out of the flow, which is proportional to the bottom TGSD and the settling velocities (yellow).

deposit, these factors would allow estimation of the true mean size of the sediment in transport during the flow event. This information would be valuable for accurately reconstructing the dynamics of the flow and sediment transport conditions from preserved deposits.

Finally, the tool also computes a depth- and solid-averaged velocity, defined as

$$\hat{u} = \frac{1}{H\overline{\rho}}\int_0^H u(z)\rho(z)dz. \tag{25}$$

This “effective” velocity has the advantage that, when multiplied by the depth-averaged density and the thickness, provides the correct mass flow rate (mfr), that is,

$$\text{mfr} = \overline{\rho}\,\hat{u}H. \tag{26}$$

3.2. Application to Depth-Averaged Dynamic Models

Models for dilute pyroclastic flows are valuable tools for understanding flow behavior and dynamics. While fully three-dimensional multiphase PDC models offer a more comprehensive portrayal of the flow's vertical stratification and interaction between the solid and gas phases (e.g., E. Breard et al., 2019; Esposti Ongaro et al., 2007, 2011; Montanino et al., 2022; Neri et al., 2003, 2022; Valentine, 2020), these types of models remain computationally expensive and therefore have limited applicability to hazard assessment. Because of this, simplified yet reliable models remain valuable, and are often essential for probabilistic approaches, which can require executing a large number of simulations within short time frames. Several models used in hazard assessment are based on the shallow-water assumption (e.g., Bursik & Woods, 1996; de' Michieli Vitturi et al., 2023; Kelfoun, 2017; Neglia et al., 2021; Shimizu et al., 2017) with a depth-averaging of flow properties (as in the Saint-Venant equations). However, this simplification requires replacing vertical profiles with constant, averaged ones. Despite this limitation, depth-averaged models remain prevalent due to their computational efficiency and insights into dilute pyroclastic flow behavior (Tierz et al., 2024).

Here we show how the vertical profiles described in the previous sections can be implemented in depth-averaged models, by introducing ad-hoc modifications to the flux terms of the depth-averaged equations. More specifically, we apply the computation of the vertical profiles to an existing shallow-water model for dilute PDC's, based on IMEX-SfloW2D (de' Michieli Vitturi et al., 2019, 2023). The numerical scheme implemented in IMEX-SfloW2D solves the conservation equations for mass (for the mixture and the individual solid phases), momentum, either total energy or thermal energy, and progresses through each time step. The existing model also contains terms within the conservation equations that account for basal erosion, sedimentation of particles, and entrainment of atmospheric air. The model assumes that the flow propagates at atmospheric pressure and that the effects of compressibility are negligible (de' Michieli Vitturi et al., 2023). For the sake of simplicity, we only report here the 1D conservation equations for mixture and solid mass, respectively, and for momentum, with constant vertical profiles assumed for horizontal velocity u and volume fraction of particles α_s, as:

$$\begin{cases} \frac{\partial}{\partial t}(\rho_m h) + \frac{\partial}{\partial x}(\rho_m u h) = -S + E \\ \frac{\partial}{\partial t}(\rho_s \alpha_s h) + \frac{\partial}{\partial x}(\rho_s \alpha_s u h) = -S \\ \frac{\partial}{\partial t}(\rho_m u h) + \frac{\partial}{\partial x}(\rho_m u^2 h) = -\frac{\partial}{\partial x}\left(\rho_m g' \frac{h^2}{2}\right) - \rho_m g' h \frac{\partial B}{\partial x} - S u + F \end{cases} \tag{27}$$

with mixture density ρ_m, solid density ρ_s, atmospheric density ρ_a, flow thickness h, sedimentation rate S, entrainment rate E, reduced gravity, defined as $g' = g \cdot \frac{\rho_m - \rho_a}{\rho_m}$, topographic elevation B, friction F. Additional equations for conservation of energy and transport of other phases/components are included in the model but not shown here, and can be found in de' Michieli Vitturi et al. (2023). The model accounts only for the suspended load region of the flow, and does not account for interactions between the bed load and suspended load.

3.2.1. Flux Modification

When non-uniform vertical profiles are introduced in the depth-averaging process producing the shallow-water equations, some multiplying coefficients appear in several terms of the equations. For example, for open channels flows, Boussinesq (1877) introduced a constant momentum coefficient β, also known as the Boussinesq factor or shape factor, accounting for the excess momentum flux with respect to that computed with the square of the depth-averaged velocity. In Biagioli et al. (2021), the assumptions of a parabolic velocity profile and a piecewise-linear temperature profile lead to the appearance of a two shape factors inside the advective terms of the momentum and temperature equations, respectively. Here we further extend the idea by introducing our own coefficients into the shallow-water equations. These coefficients are not constant, and are dynamically computed from the flow variables. With this approach, the vertical structure of the flow is also modeled and, for this reason, we use the term "2.5D" for the resulting model.

We demonstrate here how to derive the coefficients for the conservation equation for mass, which is obtained by integrating over the thickness of the flow the 3D equation:

$$\frac{\partial \rho_m}{\partial t} + \nabla \cdot (\rho_m \mathbf{u}) = 0. \tag{28}$$

For a 1D flow, by using the proper boundary conditions at the top and bottom of the flow accounting for air entrainment and particle sedimentation, the following 1D conservation equation for mass is obtained:

$$\frac{\partial}{\partial t}(\overline{\rho}_m h) + \frac{\partial}{\partial x}(\overline{\rho_m u} h) = -S + E, \tag{29}$$

where

$$\overline{\rho_m u} h = \int_B^{B+h} \rho_m u \, \mathrm{dz}. \tag{30}$$

When the velocity and the solid volume fraction vertical profiles are constant, we can omit the bar notation and use the known values to compute the flux. In the case of non-constant profiles we compute the flux in terms of the depth-averaged values $\bar{\rho}_m$ and $\bar{u}$, by introducing a coefficient ξ_1 such that:

$$\overline{\rho_m u}h = \xi_1 \bar{\rho}_m \bar{u} h, \tag{31}$$

where ξ_1 can be computed as:

$$\xi_1 = \frac{h \int \rho_m u}{\int \rho_m \cdot \int u}. \tag{32}$$

The key point in the coefficient derivation is the difference between the depth-averaged values of velocity and density, and the depth-averaged *product* of velocity and density. With this notation, the modified equation for the mass becomes

$$\frac{\partial}{\partial t}(\bar{\rho}_m\, h) + \frac{\partial}{\partial x}(\xi_1 \bar{\rho}_m \bar{u} h) = -S + E. \tag{33}$$

Please note that, differently from the Boussinesq factor, the coefficient ξ_1 changes in space (and in time), and therefore cannot be factored out of the differentiation. In a similar way, the fluxes for the other conservation equations are modified by introducing new parameters ξ_2, and ξ_3, to account for the inclusion of vertical profiles

$$\xi_2 = \frac{h \int \rho_s \alpha_s u}{\rho_s \int \alpha_s \cdot \int u}, \qquad \xi_3 = \frac{\int \rho_m u^2}{\int h^2 \rho_m \cdot \int u \cdot \int u}. \tag{34}$$

Then, the governing equations (Equation 27) become:

$$\begin{cases} \dfrac{\partial}{\partial t}(\bar{\rho}_m\, h) + \dfrac{\partial}{\partial x}(\xi_1 \bar{\rho}_m \bar{u} h) = -S + E \\ \dfrac{\partial}{\partial t}(\rho_s \bar{\alpha}_s h) + \dfrac{\partial}{\partial x}(\xi_2 \rho_s \bar{\alpha}_s \bar{u} h) = -S \\ \dfrac{\partial}{\partial t}(\overline{\rho_m u}\, h) + \dfrac{\partial}{\partial x}(\xi_3 \bar{\rho}_m \bar{u}^2 h) = -\dfrac{\partial}{\partial x}\left(\bar{\rho}_m g' \dfrac{h^2}{2}\right) - \bar{\rho}_m g'\, h \dfrac{\partial B}{\partial x} - S\, \bar{u} + F \end{cases} \tag{35}$$

The modifying coefficients ξ_i represent the excess fluxes with respect to those computed using the depth-averaged values of velocity and solid concentration. Similar coefficients also appear in the other conservation equations not presented here. It is worth noting that the conservative variable of the momentum equation is not the product of the depth-averaged density and velocity, as in the original equation, but the depth-averaged momentum. That means that when the governing equations are integrated, the values of $\bar{\rho}_m$ and $\bar{u}$ must be computed from the new conservative variables, and then the flux-modifiers can be computed by evaluating, either analytically or with a quadrature formula, the integrals in Equations 32 and 34. This is done with an iterative procedure, as described in the previous section, implemented in new subroutines of the Fortran code. With respect to the Python notebook presented in the previous section, in the shallow-water Fortran code, all the integrals needed to compute the flux modifiers are computed with a quadrature formula, which only needs the functions defining the normalized profiles for the velocity and the solid classes volume fractions. The updated model, with flux modification parameters, and a flag to enable or disable the use of the vertical profiles computed above, is currently available on GitHub (https://github.com/demichie/IMEX_SfloW2D_v2).

4. Results

We tested the differences between the original depth-averaged model and the updated version that includes vertical profiles for velocity and particle volume fraction using a 1D test case on a constant slope and a 2D test case on a real topography. Both the examples are available in the code repository.

Table 2
Simulation Parameters for the Reference Simulation (Run 0) of the 1D Test Case

Particle parameters	Symbol	Value	Units
Particle Density	ρ_s	1,750	kg/m^3
Particles Specific Heat	C_s	1,617.0	$J/(kgK)$
Particle Diameter	D	2.5×10^{-4}	m
Gas transport parameters	Symbol	Value	Units
Specific Heat Air	C_{atm}	998.0	$J/(kgK)$
Gas Constant	R	287.0510	$J/(kgK)$
Kinematic Viscosity	ν	1.48×10^{-5}	m^2/s
Atmospheric Pressure	P_{atm}	101,300.0	Pa
Ambient Temperature	T	300.0	K
Flow properties	Symbol	Value	Units
Friction Coefficient	C_f	3×10^{-3}	
Substrate Roughness	k_s	1.5	m
Inlet thickness	h_0	100	m
Inlet velocity	u_0	50 (66.93)	m/s
Inlet Temperature	T_0	900	K
Inlet solid volume fraction	$\alpha_{s,0}$	0.01	

Note. The test case Run 1 has the same inlet conditions, while Run 2 has a different velocity, reported in parenthesis.

4.1. 1D Test Case

For the 1D test case we consider a 5 km domain with a constant slope of 3° and a supercritical flow. For the sake of simplicity, only one particle class is considered here, with diameter 2.5×10^{-4} m ($\phi = 2$) and density 1,750 kgm^{-3}, which were chosen as reasonable estimations for vesicular ash particles. All the other simulation parameters are reported in Table 2. For all the simulations, the solution is initialized in the domain with thickness $h = 0$ m and velocity $u = 0$ ms^{-1}, and an influx from the left. The flow enters the domain and after a variable time, dependent on the simulation case but smaller that 180 s for all the runs presented here, reaches a steady state. The maximum runout corresponds to the point where the mixture becomes positively buoyant, because of particle sedimentation and heating of the entrained atmospheric air.

In Figure 5, we can see the steady solution, in terms of free surface $w = b + h$, for three runs. The first run (Run 0), denoted by a blue solid line, is the solution of a model simulation with constant vertical profiles, thus corresponding to the classical depth-averaged approach. For this case, after the first few hundreds of meters where the flow thickness is approximately constant and close to the inlet value, we observe an increase in flow thickness associated with the entrainment and heating of atmospheric air. Here, following Bursik and Woods (1996) and de' Michieli Vitturi et al. (2023), entrainment is a function of the Richardson number $Ri = g'h/u^2$, which is computed from the depth-averaged values of the flow variables. After 4 km, the flow thickness is almost twice the initial value and the flow becomes buoyant, thus giving the maximum runout for this case.

For the second simulation (Run 1), represented with a purple dashed line in Figure 5, we used the flux modifications for the non-constant vertical profiles and, at the inlet, the same depth-averaged values of the first run for the velocity and the solid concentration. This means that also the Richardson number is the same for the two runs at the inlet, and this results in a similar thickness in the first hundreds of meters. Despite that, we can see that the runout, at the steady state condition, is smaller, almost by a factor of two. This is due to the fact that, when the vertical profiles are considered, the inlet mass flow rates for the two simulations are different, with that of Run 1 being smaller. For both the runs, the inlet mixture density is 17.89 kgm^{-3}, which results in an inlet mass flow rate of 894.41 kgs^{-1} for the run with constant profiles. When the vertical profiles are considered, their non-linearity

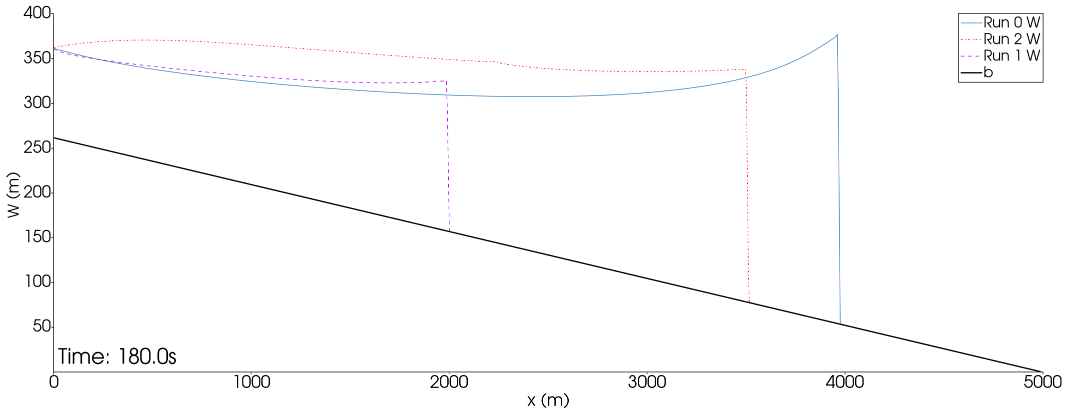

Figure 5. Free surface height $w = b + h$ plotted for three simulations run on a constant topographic slope, b, and height h using input parameters from Table 2: the blue solid line is for Run 0, with constant vertical profiles for all the variables; the purple line is for Run 1, where the variable vertical profiles are considered and where the depth-averaged values of solid volume fraction and velocity are the same of Run 0; the dotted red line is for Run 2, where the variable vertical profiles are considered but the simulation has the same depth-averaged inlet mass flow rate of Run 0, instead of the same velocity.

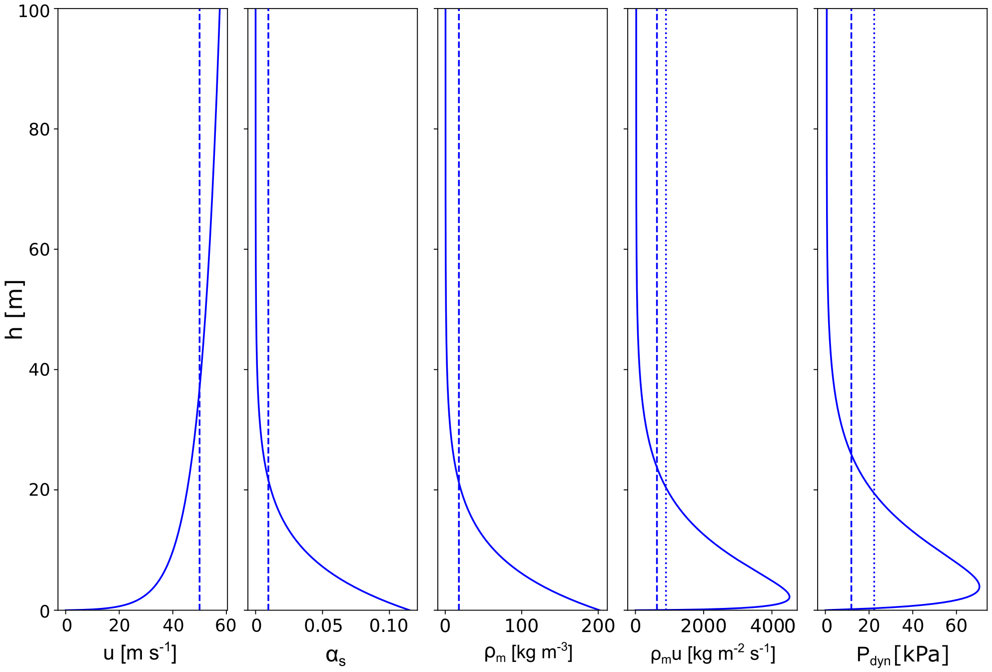

Figure 6. Vertical profiles computed from inlet conditions (Table 2). The solid lines represent the profiles for Run 1, that is, for the run with $\overline{u} = 50$ ms^{-1} and with the variable vertical profiles. The dashed lines represent the depth-averaged values of the variable plotted in each panel, while the dotted lines represent the values computed from the depth-averaged values of the solid volume fraction and the velocity.

gives an inlet mass flow rate of 630.37 kgs^{-1}, which is approximately 70% of the inlet mass flow rate of the first run. The differences at the inlet are also shown in Figure 6, where the vertical profiles are shown with solid lines for the second run. The plots are the output of the Python script described in the previous section, using the parameters those reported in Table 2 as inputs. In some panels, we also show with dashed lines the depth-averaged values of the variables plotted, and with dotted lines the values obtained from the depth-averaged values of velocity and solid volume fraction. Thus, in the panel for the mass flux $\rho_m u$, the dotted line represents the inlet mass flow rate for the first run with constant profiles for velocity and solid volume fraction (i.e., it is simply the product of the two depth-averaged values), while the dashed line represents the depth-averaged value of the inlet mass flow rate for the second run (i.e., the depth-averaged value of the solid line). We can see that for $\rho_m u$, the depth-averaged value is smaller than the product of the two depth-averaged values ($\overline{\rho}$ and $\overline{u}$). It is also interesting to note that a significant difference in the dynamic pressure can be observed in the lower portion of the flow, with the simulation with constant vertical profiles (dotted line) largely underestimating the peak shown in the variable profile (solid line).

Because the first two runs described in this section have different inlet rates, a third run (Run 2) was performed with the same mass flow rate of the first one. The steady-state profile of thickness versus distance is plotted with a red dashed line in Figure 5. Here, to produce the desired mass flow rate, we kept fixed all the parameters listed in Table 2, except for the inlet velocity, which was increased to 66.93 ms^{-1}. This results in a smaller Richardson number, and thus in a larger entrainment rate, which produces an increase in flow thickness with respect to the reference run. The higher mass flow rate increases the final runout distance with respect to Run 1 (purple dashed line), but the larger entrainment, with the associated decrease in density, prevents the run from reaching the same runout as Run 0, with the difference between Run 2 and Run 0 being approximately 400 m.

Finally, in Figure 7, we show the values of the variables for Run 0 and Run 2 (the two runs with same mass flow rate at the inlet) at a probe located at $x = 3000$ meters, when the steady condition is reached for both the simulations. The blue lines are for Run 2 (with dashes for depth-averaged values), while the red lines are for Run 0. The extent of the vertical axis in the panels corresponds to the thickness of the flow at the probe location for Run 2. By looking at the first two panels, representing the values of the two variables for which the vertical profiles have

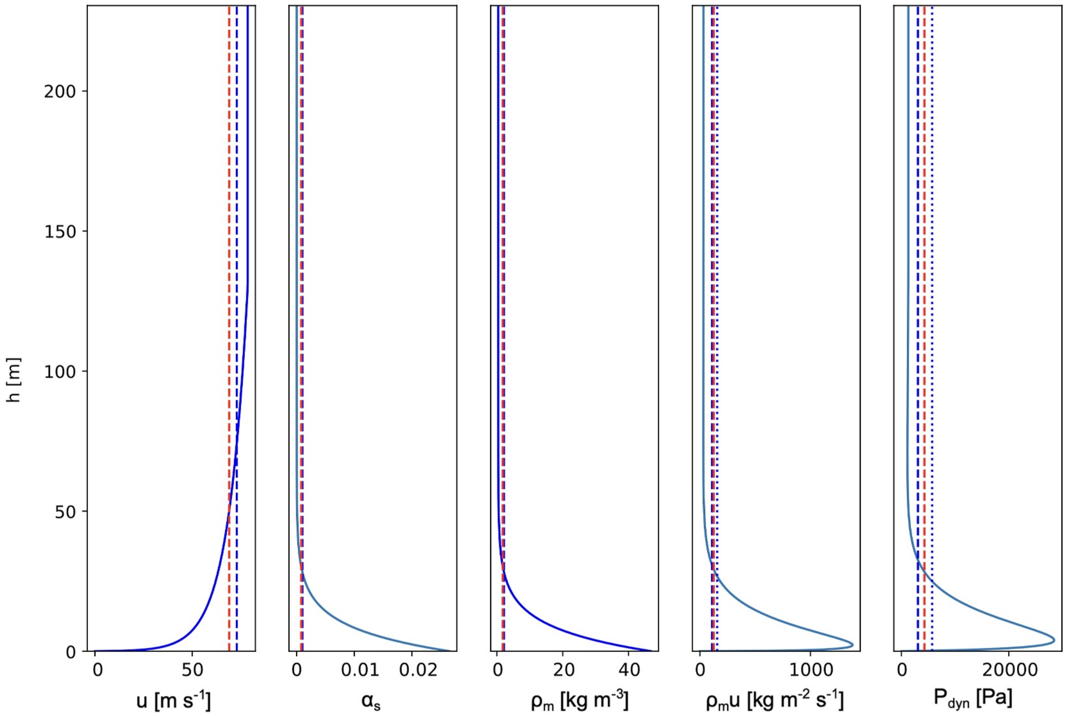

Figure 7. Vertical profiles for flow properties computed at x = 3,000 m. The red lines are for Run 0, that is, the run with $\overline{u} = 50\ \mathrm{ms}^{-1}$ and with the constant vertical profile, while the blue lines are for Run 2, that is, for the run with $\overline{u} = 66.93\ \mathrm{ms}^{-1}$ and with the variable vertical profiles. Please note that the two runs have the same inlet mass flow rate. For Run 2, the dashed lines represent the depth-averaged values of the variable plotted in each panel, while the dotted lines represent the values computed from the depth-averaged values of the solid volume fraction and the velocity.

been implemented (velocity and solid volume fraction), we can see that the difference in the depth-averaged solid fractions is negligible, while the difference in the depth-averaged velocities is larger, with the value for Run 2 exceeding that of Run 0. These differences result also in a difference in the average dynamic pressure, which is smaller for Run 2 than Run 0, as shown by the dashed lines in the last panel of Figure 7. This is due to the non-linear dependence of the dynamic pressure on the velocity and solid volume fraction, and the fact that in the lower portion of the flow the velocity for Run 2 is smaller than that of Run 0. More importantly, looking at the peak in the dynamic pressure, we can see that its value is much larger than the constant value obtained with the constant profiles. This large difference between the two simulations has a significant impact on hazard assessment, showing that neglecting the vertical variations in flow profiles, as is usually done with depth-averaged models, can largely underestimate the hazard associated with a flow.

4.2. 2D Test Case

The second test case presented in this work is an application of the model to a real topography. Here, we apply the updated model to generate a set of probabilistic hazard maps for the Maungataketake tuff ring area, which is part of a nested volcanic complex located near the Manukau Harbour in southern Auckland City (New Zealand) that erupted between 180 and 200 ka. In Brand et al. (2014), field observations constrained the runout distance, dynamic pressure, and temperature of the eruption, which were then used with the original Bursik and Woods (1996) model to obtain an estimation of the initial eruptive conditions. Using this model, they attempted to match flow dynamic pressures at various distances and deposit extent for one of the phreatomagmatic packages of the Maungataketake tuff ring by adjusting the bulk density, the velocity and the initial thickness within plausible ranges.

Here, to generate the hazard maps for the Maungataketake region, a probabilistic approach was employed to account for uncertainties in the eruption source parameters. First, a range of plausible values was defined for the mass flow rate (2.0×10^8 to 1.0×10^9 kg/s), solid mass fraction (0.95–0.98), and temperature (700–

900 K) of the pyroclastic surge based on the calibration simulations and field observations from Brand et al. (2014). Then, a Monte Carlo sampling algorithm was used to generate a set of input parameters for 200 simulations. We sampled the mass flow rate using a log-linear distribution, and the solid mass fraction and temperature using linear distributions within their respective ranges. For all the simulations, the source conditions were given with a radius $R = 200$ m, with the initial Richardson number fixed at $Ri = 0.5$. For each set of sampled input parameters, a 2D transient simulation was performed using the updated model with vertical profiles, considering the actual topography of the Maungataketake region and running for a sufficient duration to ensure that the pyroclastic surge reached its maximum runout distance (50 s). The results of all simulations were combined to create probability maps of the invasion area, displaying the likelihood of a given location being affected by the pyroclastic surge based on the proportion of simulations that resulted in the flow reaching that location. Additionally, separate hazard maps were created for specific thresholds of dynamic pressure, showing the probability of a location experiencing dynamic pressures exceeding critical values that could cause damage to infrastructure or pose a risk to human life. These probabilistic hazard maps provide a comprehensive assessment of the potential impact of a pyroclastic surge event similar to the one that formed the Maungataketake tuff ring, considering uncertainties in the source parameters and utilizing the updated model with vertical profiles to offer a more realistic and informative tool for hazard assessment and decision-making in the region.

In Figure 8, the temporal evolution of one simulation of the Monte Carlo ensemble is shown. For this specific run, the mass flow rate is 6.71×10^8 kg s^{-1}, the solid mass fraction is 0.966, and the temperature is 731.2 K. These input values, with the Richardson number fixed at the inlet with a value of $Ri = 0.5$, and the source radius of 200 m, allow the code to automatically compute the flow height and velocity at the source. The figure shows a map of flow thickness at 5, 15, 25, and 50 s, respectively. In the last panel a steady condition is reached, and the maximum runout distance is approximately 2.8 km. We can also see the gentle slope has a negligible effect on the flow propagation, with a similar runout in all the directions. Here, the average velocity of the flow front is 50 m/s. For the same run, Figure 9 shows the vertical profiles, at $t = 25$ seconds, for different flow parameters plotted at the two probes presented in the top-left panel of Figure 8. The distance between the probes is approximately 400 m and their locations were selected to examine the effects of the flow moving over a large structure, which can be seen in the topography, and is approximately 14 m high. Between the two probes, the flow thickens from 137 to 145 m, both due to the effects of atmospheric entrainment and the perturbation from the topographic obstacle. The maximum dynamic pressure also decreases between the two probe locations, primarily due to a decrease in the velocity of the flow, and secondarily a decrease in the flow density due to atmospheric entrainment and particle sedimentation.

The temperature, height, and mixture density of the flow is plotted in Figure 10 along the transect in the bottom right panel of Figure 8 at $t = 50$ s. Important trends to note in these three flow parameters are that the height of the flow decreases rapidly at the inlet, but then gradually increases with distance from source. The wavy appearance of the flow height line is a result of flow interaction with local topography. The superposition of thinning from radial spreading and thickening from atmospheric air entrainment causes these two different trends. Thinning is more significant near the source, while thickening becomes more prominent at greater distances (Calabrò et al., 2022; de' Michieli Vitturi et al., 2023). The density of the flow also has a maximum at the inlet, and decreases with distance from source due to both atmospheric entrainment and particle sedimentation. Note that here, the density plotted is the depth-averaged value. Finally, in the bottom panel we can see that the temperature of the flow is decreasing with distance, again due to entrainment of cooler atmospheric air, as well as loss of the initially hot volcanic particles due to sedimentation. These results accurately capture the physical processes present in these types of flows.

Finally, in Figure 11, we can see the probabilistic hazard maps for flow runout (top row) and exceeding a dynamic pressure threshold of 1 kPa (bottom), which is not necessarily the absolute maximum, but rather the dynamic pressure computed 2 m above the basal boundary. The left column shows the model output with the updated vertical profiles, and the right column computes the dynamic pressure from the depth-averaged values. Figure 11 clearly demonstrates that while the two versions of the model produce similar runout distances, the extent of the 1 kPa dynamic pressure, which represents the lowest threshold for possible damage (Dellino, Dioguardi, Isaia, et al., 2021), is underestimated using only the depth-averaged values. These results demonstrate that the new model, and methodology could have a significant impact for hazard assessment. The maps presented here are not

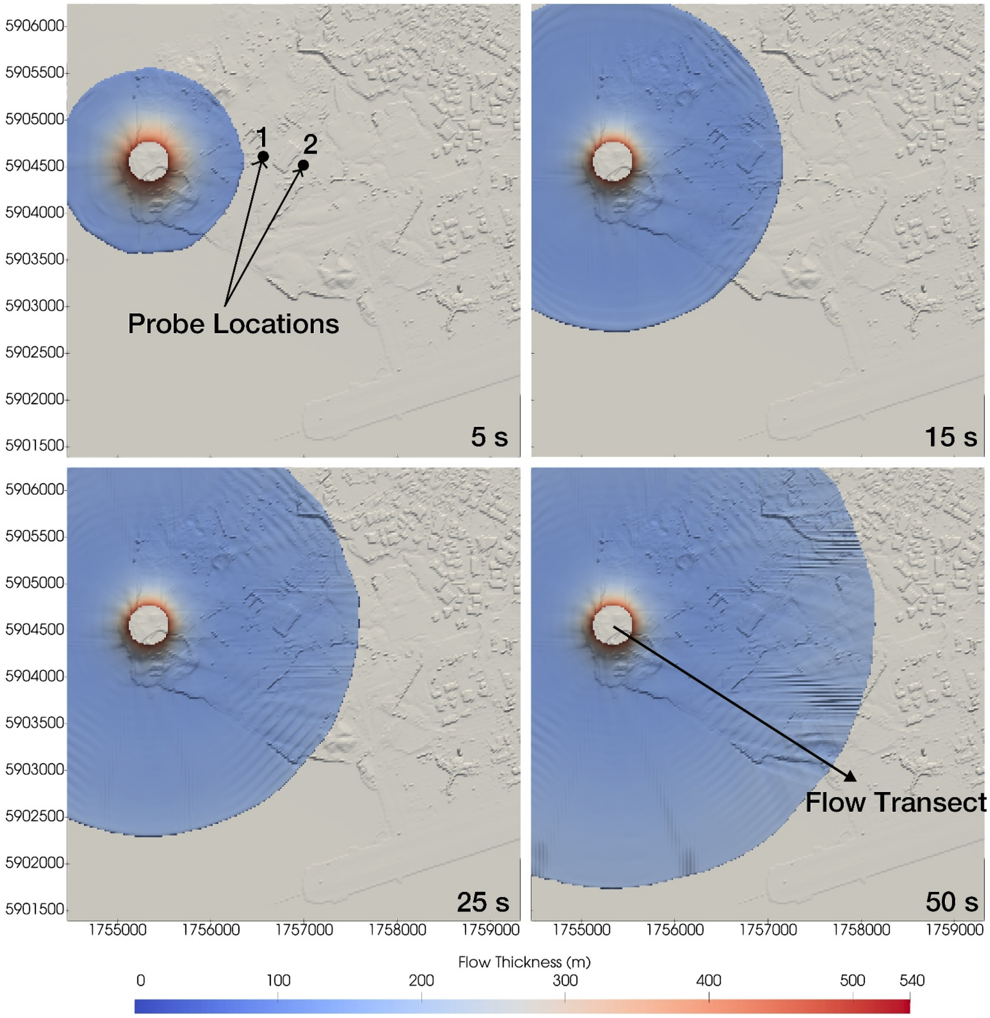

Figure 8. Flow height through time, plotted at 5, 15, 25, and 50 s. Data from ensemble simulation number 1 of 200. Note probe locations in the upper right panel, separated by a distance of 400 m, located before and after a large building that is approximately 14 m tall. Flow transect in the bottom right panel is used to generate line plots used in Figure 9.

intended for operational use or land-use planning; they merely illustrate the potential differences that can arise from employing the new depth-averaged model.

5. Conclusions

We have presented a new approach for computing vertical profiles of velocity and particle volume fraction in dilute pyroclastic density currents using depth-averaged values and non-dimensional flow parameters. We then showed how these profiles can be implemented in shallow-water models, by modifying the flux terms of the governing equations. These modifications were implemented in the open–source code IMEX-SfloW2D, and we compared the updated model results to those of the original depth-averaged model for both a 1D gentle slope case and a 2D case on a real topography. The 1D test case highlighted that the depth-averaged value of the velocity does not represent the best choice of an input value for a simulation with a shallow-water model. This is because it does not necessarily result in the correct mass flow rate, since the depth-average value of this variable is different from the product of the depth-averaged density and velocity. A better option would be to compute an effective depth and solid-averaged velocity, as defined by Equation 25 and computed by the Python code, or to provide directly the depth-averaged mass flow rate.

Both the test cases show that the modifications made here to the depth-averaged model, to include vertical profiles for velocity and concentration, allow for a more accurate physical description for the dynamics of pyroclastic

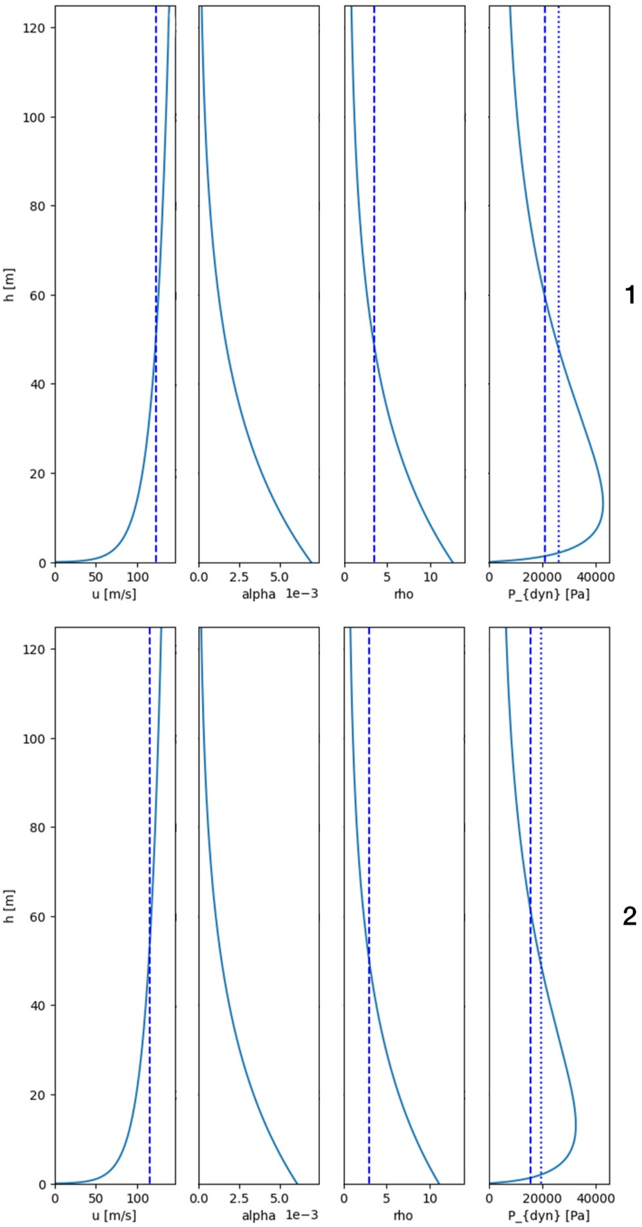

Figure 9. Profiles of flow parameters at probe location 1 (top) and 2 (bottom). Dashed lines represent the depth-averaged values of the variables plotted, and dotted lines represent the values obtained from the depth-averaged values of velocity and solid volume fraction.

surges and a better estimation of their dynamic pressure. This model also still retains reasonable computation times despite its increased complexity. This low computational cost means that the model can be a valuable tool for probabilistic hazard assessment, as done for the for the 2D test case. The profiles detailed in this paper have been implemented in the IMEX-SfloW2D code - however it is important to note that the method of flux correction used here can be added to any depth-averaged code.

The Python tool described here contains everything needed for computation of the vertical profiles from depth-averaged values and can also be used as a forensic tool to associate properties of the deposit to flow properties, as done in Dellino, Dioguardi, Rinaldi, et al. (2021). As shown in Figure 4, the tool allows the user to compute the ratios between the total grain size distribution within the flow and that of the particles lost at the base of the flow. The ratios between these mean sizes can be used as correction factors to infer, from the mean grain size of a

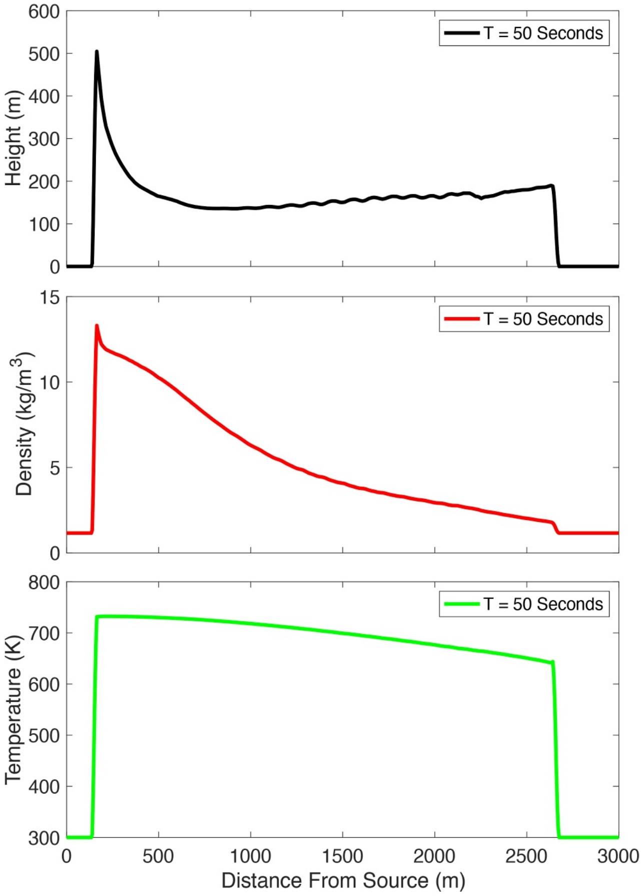

Figure 10. Line plot of flow height, temperature, and mixture density with distance from source for ensemble simulation number 1 of 200. Please note that the source is at a distance of 200 m from the origin. Also note that the density plotted in the middle panel is the depth-averaged value, and is not based on the new vertical profiles.

deposit, the true mean size of the particles in transport during the flow event. In addition, it is possible to combine the tool with optimization and root finding libraries to associate the peak of dynamic pressure, or its value at a fixed height within the flow, to the depth-averaged velocity, or the depth-averaged mass flow rate.

As previously stated, it is important to acknowledge that the proposed vertical profiles represent a simplified representation of the complex flow dynamics of pyroclastic surges. In reality, turbulent flows exhibit continuous fluctuations in the vertical profiles. The profiles presented here are approximations of time-averaged conditions, where the effects of turbulence are averaged over time. We are working on adding a stochastic transport equation in the model, that could be used to add turbulent effects. So far it has been used to introduce a new friction model depending on this fluctuating variable, but in the future the stochastic fluctuation could also be accounted for in the velocity profiles or in the dynamic pressure computation. In any case, the use of vertical profiles for velocity and particle volume fraction are not limited to the profiles that we have assumed. Further modification could allow for the use of other types of profiles, such as those proposed by Cerminara et al. (2021), through a similar method of flux modification and iterative calculation.

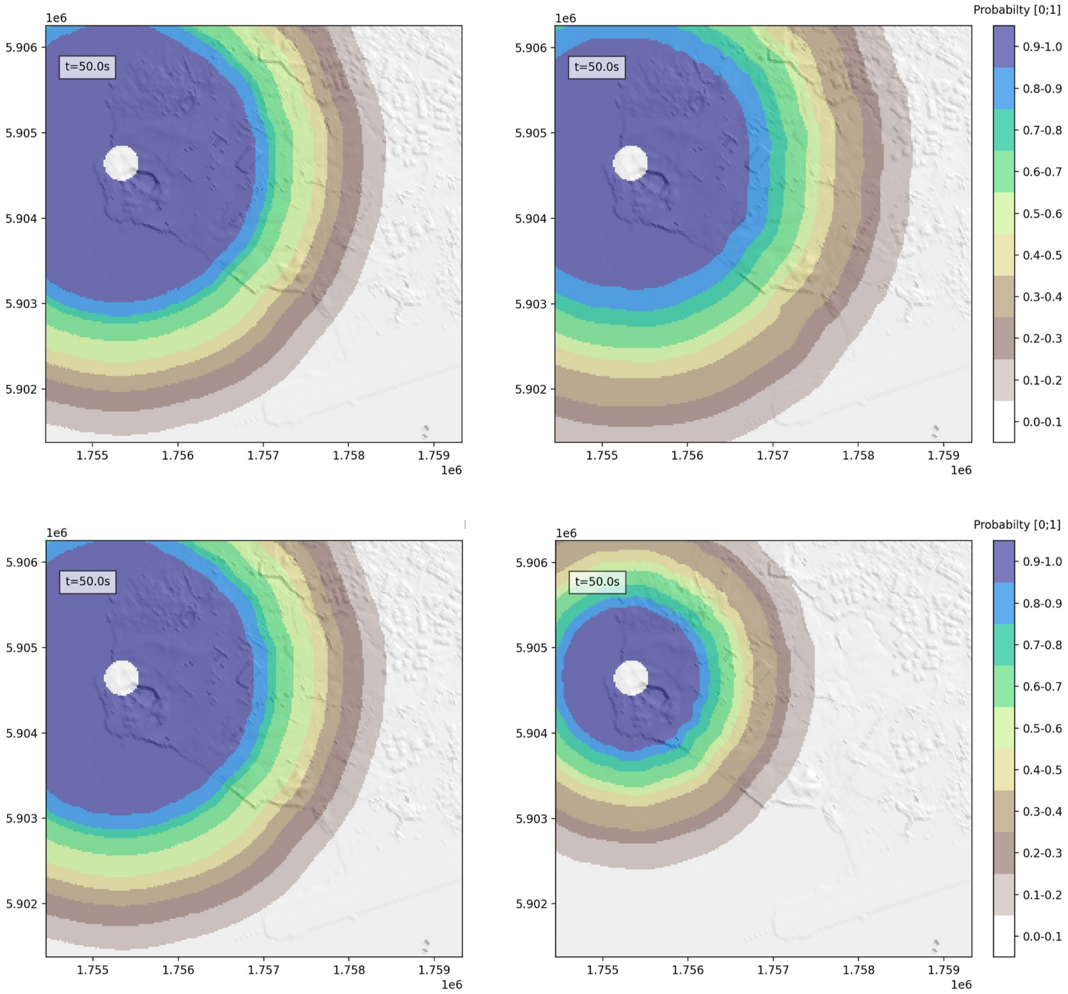

Figure 11. Top row: Probabilistic hazard map for Maungataketake, NZ, for invasion/maximum flow runout in models with (left) and without (right) the updated vertical profiles. Bottom row: probabilistic hazard map for maximum dynamic pressures exceeding 1,000 Pa computed with (left) and without (right) the updated vertical profiles. The dynamic pressure for the model with the updated profiles is calculated at a height of 2 m.

Appendix: Derivation of the Vertical Profiles Terms A

A1. Boundary Layer Height d_{bl}

To find the boundary layer height, d_{bl}, we solve the following equation:

$$\frac{1}{H}\int_0^{d_{bl}} u(z)dy = 1. \tag{A1}$$

Substituting the relative velocity profile, $\frac{u(z)}{U}$, gives:

$$\frac{1}{H}\left[d_{bl}\left(\frac{k_s}{H}+\frac{1}{30}\right)\cdot\ln\left(\frac{30d_{bl}}{k_s}+1\right)-d_{bl}+(H-d_{bl})\cdot\ln\left(\frac{30d_{bl}}{k_s}+1\right)\right]=\frac{\kappa}{\sqrt{C_f}}. \tag{A2}$$

Collecting and simplifying terms yields:

$$\frac{k_s}{H}\left(\frac{1}{30}+\frac{H}{k_s}\right)\cdot\ln\left(\frac{30d_{bl}}{k_s}+1\right)-\frac{d_{bl}}{k_s}=\frac{\kappa}{\sqrt{C_f}}. \tag{A3}$$

Introducing the following substitution variables:

$$a=\frac{\frac{H}{k_s}\sqrt{C_f}}{\kappa},\qquad b=\frac{1}{30}+\frac{H}{k_s},\qquad c=30, \tag{A4}$$

the equation can be written in the equivalent form:

$$a=b\ln\left(c\cdot\frac{d_{bl}}{k_s}+1\right)-\frac{d_{bl}}{k_s}. \tag{A5}$$

The solution for the boundary layer height d_{bl} is:

$$d_{bl}=-bk_s\cdot\mathcal{W}\left(-\frac{e^{\frac{a}{b}-\frac{1}{bc}}}{bc}\right)-\frac{1}{c}, \tag{A6}$$

where $\mathcal{W}$ is the Lambert-W function.

A2. Sediment Diffusivity

The value of ϵ_s is obtained by assuming a linear relationship between mass and momentum diffusivity ($\epsilon_s \approx \beta_{sm}\epsilon_m$, where β_{sm} is the Schmidt number), with the latter related to the shear stress τ and the velocity profile $u(z)$ through the following equation:

$$\frac{\tau(z)}{\rho}=\epsilon_m\frac{du(z)}{dz}. \tag{A7}$$

In the turbulent boundary layer the velocity gradient, based on the previously derived velocity profile, is given by:

$$\frac{du(z)}{dz}=\frac{30u_*}{\kappa\cdot(30z+k_s)}. \tag{A8}$$

In addition, according to the Law of the Wall, in the turbulent boundary layer the shear stress varies linearly between τ_b and 0, and thus it can be written as

$$\tau(z)=\tau_b\frac{d_{bl}-z}{d_{bl}}. \tag{A9}$$

Then, combining Equations A7–A9 gives:

$$\frac{\tau_b\left(\frac{d_{bl}-z}{d_{bl}}\right)}{\rho}=\epsilon_m\cdot\left(\frac{30u_*}{\kappa\cdot(30z+k_s)}\right). \tag{A10}$$

Substituting in Equation 5 for the definition of the basal stress τ_b transforms Equation A10 into:

$$u_*^2\left(\frac{d_{bl}-z}{d_{bl}}\right)=\epsilon_m\cdot\left(\frac{30u_*}{\kappa\cdot(30z+k_s)}\right). \tag{A11}$$

Solving for ϵ_m gives:

$$\epsilon_m = u_* \cdot \kappa \cdot \left(z + \frac{k_s}{30}\right) \cdot \left(\frac{d_{bl} - z}{d_{bl}}\right). \tag{A12}$$

Integrating from 0 to d_{bl} gives the depth-averaged diffusivity:

$$\bar{\epsilon}_m = \frac{1}{d_{bl}} \int_0^{d_{bl}} \epsilon_m \, dz = \kappa u_* \left(\frac{d_{bl}}{6} + \frac{k_s}{60}\right), \tag{A13}$$

which gives us the depth-averaged sediment mass diffusivity as:

$$\bar{\epsilon}_s = \beta_{sm} \kappa u_* \left(\frac{d_{bl}}{6} + \frac{k_s}{60}\right). \tag{A14}$$

A3. Calculating C_{coeff}

C_{coeff} is computed as a normalization of the integral of the concentration profile, so we have

$$C_{coeff} = \frac{1}{\int c(z) dz}. \tag{A15}$$

We analytically compute the integral of the concentration profile as

$$\int c(z) dz = \left(\frac{e^{a \cdot d_{bl}} - 1.0}{a} + e^{(a \cdot d_{bl}) * (h - d_{bl})}\right) \cdot \frac{1}{h}. \tag{A16}$$

Note that the product of C_{coeff} and the concentration profile $c(z)$ has a depth-averaged value equal to 1.

A4. Lambert Function $\mathcal{W}$

The Lambert $\mathcal{W}$ function, denoted as $\mathcal{W}(x)$, is defined as the inverse function of $f(\mathcal{W}) = \mathcal{W}e^{\mathcal{W}}$. That is, for a given x:

$$\mathcal{W}(x) e^{\mathcal{W}(x)} = x. \tag{A17}$$

The function is multi-valued, and has two primary branches. The principal real branch, which is used in this work, is denoted as $\mathcal{W}_0(x)$ and the secondary branch as $\mathcal{W}_{-1}(x)$. The principal branch $\mathcal{W}_0(x)$ is real for $x \geq -\frac{1}{e}$. The secondary branch $\mathcal{W}_{-1}(x)$ is real for $-\frac{1}{e} \leq x < 0$. The Lambert function is used here since is the simplest representation of the integral of the velocity profile.

Data Availability Statement

Input files used for the simulations presented in this paper, and the Python tool for computing the vertical profiles, are available in Keim (2024). The Python tool is also available on Google Colab, which allows the script to be run without having Python installed locally. The modified shallow-water model IMEX-SfloW2D-V2 and examples can also be found in de' Michieli Vitturi (2023).

Acknowledgments
This work is supported by the US National Science Foundation with Grant EAR-2035260. Open access publishing facilitated by Istituto Nazionale di Geofisica e Vulcanologia, as part of the Wiley - CRUI-CARE agreement.

References

Aitken, A. C. (1927). Xxv.—On Bernoulli's numerical solution of algebraic equations. *Proceedings of the Royal Society of Edinburgh*, *46*, 289–305. https://doi.org/10.1017/s0370164600022070

Biagioli, E., de' Michieli Vitturi, M., & Di Benedetto, F. (2021). Modified shallow water model for viscous fluids and positivity preserving numerical approximation. *Applied Mathematical Modelling*, *94*, 482–505. https://doi.org/10.1016/j.apm.2020.12.036

Bonadonna, C., & Phillips, J. C. (2003). Sedimentation from strong volcanic plumes. *Journal of Geophysical Research*, *108*(B7), 2340. https://doi.org/10.1029/2002jb002034

Boussinesq, J. (1877). Essai sur la théorie des eaux courantes. *Imprimerie nationale*.

Brand, B. D., Gravley, D. M., Clarke, A. B., Lindsay, J. M., Bloomberg, S. H., Agustin-Flores, J., & Németh, K. (2014). A combined field and numerical approach to understanding dilute pyroclastic density current dynamics and hazard potential: Auckland Volcanic Field, New Zealand. *Journal of Volcanology and Geothermal Research*, *276*, 215–232. https://doi.org/10.1016/j.jvolgeores.2014.01.008

Breard, E., Dufek, J., & Roche, O. (2019). Continuum modeling of pressure-balanced and fluidized granular flows in 2-D: Comparison with glass bead experiments and implications for concentrated pyroclastic density currents. *Journal of Geophysical Research: Solid Earth*, *124*(6), 5557–5583. https://doi.org/10.1029/2018jb016874

Breard, E. C., & Lube, G. (2017). Inside pyroclastic density currents–uncovering the enigmatic flow structure and transport behaviour in large-scale experiments. *Earth and Planetary Science Letters*, *458*, 22–36. https://doi.org/10.1016/j.epsl.2016.10.016

Brosch, E., & Lube, G. (2020). Spatiotemporal sediment transport and deposition processes in experimental dilute pyroclastic density currents. *Journal of Volcanology and Geothermal Research*, *401*, 106946. https://doi.org/10.1016/j.jvolgeores.2020.106946

Brosch, E., Lube, G., Cerminara, M., Esposti Ongaro, T., Breard, E. C., Dufek, J., et al. (2021). Destructiveness of pyroclastic surges controlled by turbulent fluctuations. *Nature Communications*, *12*(1), 7306. https://doi.org/10.1038/s41467-021-27517-9

Bursik, M. I., & Woods, A. W. (1996). The dynamics and thermodynamics of large ash flows. *Bulletin of Volcanology*, *58*(2), 175–193. https://doi.org/10.1007/s004450050134

Calabrò, L., Esposti Ongaro, T., Giordano, G., & de'Michieli Vitturi, M. (2022). Reconstructing pyroclastic currents' source and flow parameters from deposit characteristics and numerical modelling: The Pozzolane Rosse Ignimbrite case study (Colli Albani, Italy). *Journal of Geophysical Research: Solid Earth*, *127*(5), e2021JB023637. https://doi.org/10.1029/2021jb023637

Cerminara, M., Brosch, E., & Lube, G. (2021). A theoretical framework and the experimental dataset for benchmarking numerical models of dilute pyroclastic density currents. *arXiv preprint arXiv:2106.14057*.

Chaudhry, M. H. (2014). *Applied hydraulic transients* (Vol. 415). Springer.

Dellino, P., Dioguardi, F., Doronzo, D. M., & Mele, D. (2019). The rate of sedimentation from turbulent suspension: An experimental model with application to pyroclastic density currents and discussion on the grain-size dependence of flow runout. *Sedimentology*, *66*(1), 129–145. https://doi.org/10.1111/sed.12485

Dellino, P., Dioguardi, F., Isaia, R., Sulpizio, R., & Mele, D. (2021). The impact of pyroclastic density currents duration on humans: The case of the AD 79 eruption of Vesuvius. *Scientific Reports*, *11*(1), 1–9. https://doi.org/10.1038/s41598-021-84456-7

Dellino, P., Dioguardi, F., Rinaldi, A., Sulpizio, R., & Mele, D. (2021). Inverting sediment bedforms for evaluating the hazard of dilute pyroclastic density currents in the field. *Scientific Reports*, *11*(1), 21024. https://doi.org/10.1038/s41598-021-00395-3

de' Michieli Vitturi, M. (2023). demichie/IMEX_SfloW2D_v2: February 9, 2024 release (version 1.0.2) [Software]. *Zenodo*. https://doi.org/10.5281/zenodo.10639237

de' Michieli Vitturi, M., Esposti Ongaro, T., & Engwell, S. (2023). IMEX_SfloW2D v2: A depth-averaged numerical flow model for volcanic gas-particle flows over complex topographies and water. *Geoscientific Model Development Discussions*, *2023*(21), 1–42. https://doi.org/10.5194/gmd-16-6309-2023

de' Michieli Vitturi, M., Esposti Ongaro, T., Lari, G., & Aravena, A. (2019). IMEX_SfloW2D 1.0: A depth-averaged numerical flow model for pyroclastic avalanches. *Geoscientific Model Development*, *12*(1), 581–595. https://doi.org/10.5194/gmd-12-581-2019

Dingman, S. L. (1984). *Fluvial hydrology* (Vol. 105, pp. 166–173). WH Freeman and Company.

Dioguardi, F., & Dellino, P. (2014). PYFLOW: A computer code for the calculation of the impact parameters of dilute pyroclastic density currents (DPDC) based on field data. *Computers & Geosciences*, *66*, 200–210. https://doi.org/10.1016/j.cageo.2014.01.013

Dioguardi, F., & Mele, D. (2018). PYFLOW_2. 0: A computer program for calculating flow properties and impact parameters of past dilute pyroclastic density currents based on field data. *Bulletin of Volcanology*, *80*(3), 1–16. https://doi.org/10.1007/s00445-017-1191-z

Doronzo, D. M., Di Vito, M. A., Arienzo, I., Bini, M., Calusi, B., Cerminara, M., et al. (2022). The 79 CE eruption of Vesuvius: A lesson from the past and the need of a multidisciplinary approach for developments in volcanology. *Earth-Science Reviews*, *231*, 104072. https://doi.org/10.1016/j.earscirev.2022.104072

Dufek, J., Ongaro, T. E., & Roche, O. (2015). Pyroclastic density currents: Processes and models. In *The encyclopedia of volcanoes* (pp. 617–629). Elsevier.

Esposti Ongaro, T., Barsotti, S., Neri, A., & Salvetti, M. V. (2011). Large-eddy simulation of pyroclastic density currents. In *Quality and reliability of large-eddy simulations II* (pp. 161–170). Springer.

Esposti Ongaro, T., Cavazzoni, C., Erbacci, G., Neri, A., & Salvetti, M.-V. (2007). A parallel multiphase flow code for the 3D simulation of explosive volcanic eruptions. *Parallel Computing*, *33*(7–8), 541–560. https://doi.org/10.1016/j.parco.2007.04.003

Esposti Ongaro, T., Cerminara, M., Charbonnier, S., Lube, G., & Valentine, G. (2020). A framework for validation and benchmarking of pyroclastic current models. *Bulletin of Volcanology*, *82*(6), 1–17. https://doi.org/10.1007/s00445-020-01388-2

Fagents, S. A., Gregg, T. K., & Lopes, R. M. (2013). *Modeling volcanic processes: The physics and mathematics of volcanism*. Cambridge University Press.

Jones, T. J., Beckett, F., Bernard, B., Breard, E. C., Dioguardi, F., Dufek, J., et al. (2023). Physical properties of pyroclastic density currents: Relevance, challenges and future directions. *Frontiers in Earth Science*, *11*, 1218645. https://doi.org/10.3389/feart.2023.1218645

Keim, B. (2024). BKeim-UB/SW_VERT_PROFILES: November 14, 2024 release (version 1.0.0) [Software]. *Zenodo*. https://doi.org/10.5281/zenodo.14163661

Kelfoun, K. (2017). A two-layer depth-averaged model for both the dilute and the concentrated parts of pyroclastic currents. *Journal of Geophysical Research: Solid Earth*, *122*(6), 4293–4311. https://doi.org/10.1002/2017jb014013

Lagmay, A. M. F., Balangue-Tarriela, M. I. R., Aurelio, M., Ybanez, R., Bonus-Ybanez, A., Sulapas, J., et al. (2021). Hazardous base surges of Taal's 2020 eruption. *Scientific Reports*, *11*(1), 15703. https://doi.org/10.1038/s41598-021-94866-2

Lube, G., Breard, E., Cronin, S., & Jones, J. (2015). Synthesizing large-scale pyroclastic flows: Experimental design, scaling, and first results from PELE. *Journal of Geophysical Research: Solid Earth*, *120*(3), 1487–1502. https://doi.org/10.1002/2014jb011666

Lube, G., Breard, E. C., Esposti-Ongaro, T., Dufek, J., & Brand, B. (2020). Multiphase flow behaviour and hazard prediction of pyroclastic density currents. *Nature Reviews Earth & Environment*, *1*(7), 348–365. https://doi.org/10.1038/s43017-020-0064-8

Middleton, G. V., & Southard, J. B. (1977). *Mechanics of sediment movement*. Society of Economic Paleontologists and Mineralogists, S.E.P.M.

Montanino, A., Franci, A., Rossi, R., & Zuccaro, G. (2022). Finite element formulation for compressible multiphase flows and its application to pyroclastic gravity currents. *Journal of Computational Physics*, *451*, 110825. https://doi.org/10.1016/j.jcp.2021.110825

Neglia, F., Sulpizio, R., Dioguardi, F., Capra, L., & Sarocchi, D. (2021). Shallow-water models for volcanic granular flows: A review of strengths and weaknesses of TITAN2D and FLO2D numerical codes. *Journal of Volcanology and Geothermal Research*, *410*, 107146. https://doi.org/10.1016/j.jvolgeores.2020.107146

Neri, A., Esposti Ongaro, T., Cerminara, M., & Cerminara, M. (2022). Multiphase flow modeling of explosive volcanic eruptions. In *Transport phenomena in multiphase systems* (pp. 243–281). Springer.

Neri, A., Esposti Ongaro, T., Macedonio, G., & Gidaspow, D. (2003). Multiparticle simulation of collapsing volcanic columns and pyroclastic flow. *Journal of Geophysical Research*, *108*(B4), 2202. https://doi.org/10.1029/2001jb000508

Pensa, A., Giordano, G., Corrado, S., & Petrone, P. P. (2023). A new hazard scenario at Vesuvius: Deadly thermal impact of detached ash cloud surges in 79CE at Herculaneum. *Scientific Reports*, *13*(1), 5622. https://doi.org/10.1038/s41598-023-32623-3

Roche, O. (2012). Depositional processes and gas pore pressure in pyroclastic flows: An experimental perspective. *Bulletin of Volcanology*, *74*(8), 1807–1820. https://doi.org/10.1007/s00445-012-0639-4

Rouse, H. (1937). Modern conceptions of the mechanics of fluid turbulence. *Transactions of the American Society of Civil Engineers*, *102*(1), 463–505. https://doi.org/10.1061/taceat.0004872

Shimizu, H. A., Koyaguchi, T., & Suzuki, Y. J. (2017). A numerical shallow-water model for gravity currents for a wide range of density differences. *Progress in Earth and Planetary Science*, *4*, 1–13. https://doi.org/10.1186/s40645-017-0120-2

Sigurdsson, H., Houghton, B., McNutt, S., Rymer, H., & Stix, J. (2015). *The encyclopedia of volcanoes*. Elsevier.

Swanson, D. A., Weaver, S. J., & Houghton, B. F. (2015). Reconstructing the deadly eruptive events of 1790 CE at Kīlauea Volcano, Hawai ʻi. *Bulletin*, *127*(3–4), 503–515. https://doi.org/10.1130/b31116.1

Tierz, P., Spiller, E. T., Clarke, B. A., Dessalegn, F., Bekele, Y., Lewi, E., et al. (2024). Topographic controls on pyroclastic density current hazard at Aluto volcano (Ethiopia) identified using a novel zero-censored Gaussian Process emulator. *Journal of Geophysical Research: Solid Earth*, *129*(5), e2023JB028645. https://doi.org/10.1029/2023jb028645

Valentine, G. A. (1987). Stratified flow in pyroclastic surges. *Bulletin of Volcanology*, *49*(4), 616–630. https://doi.org/10.1007/bf01079967

Valentine, G. A. (1998). Damage to structures by pyroclastic flows and surges, inferred from nuclear weapons effects. *Journal of Volcanology and Geothermal Research*, *87*(1–4), 117–140. https://doi.org/10.1016/s0377-0273(98)00094-8

Valentine, G. A. (2020). Initiation of dilute and concentrated pyroclastic currents from collapsing mixtures and origin of their proximal deposits. *Bulletin of Volcanology*, *82*(2), 20. https://doi.org/10.1007/s00445-020-1366-x

Von Kármán, T. (1931). *Mechanical similitude and turbulence (No. 611)*. National Advisory Committee for Aeronautics.